Research Article | Vol. 25, No. 15 | 24 Jul 2017 | OPTICS EXPRESS 17201
Optics EXPRESS

Real-time dynamic sensing with an on-chip nanophotonic sensor

YAZHAO LIU[1] AND H. W. M. SALEMINK[1,2,*]

[1]*Faculty of Civil Engineering and Geosciences, Geosciences and Engineering, Delft University of Technology, 2628 CN, Delft, The Netherlands*
[2]*Institute for Molecules and Materials, Radboud University Nijmegen, Heijendaalseweg 135, 6525 AJ, Nijmegen, The Netherlands*
[*]*h.salemink@science.ru.nl*

Abstract: We demonstrate a nanophotonic sensor for real-time monitoring of fluid flows. The sensor is based on a silicon photonic crystal cavity with a well aligned micro fluidic channel for fluid-injection. The simulated resonant wavelength shift of the sensor with residual oil in holes is 9.0 nm, and the observed experimental shift under the same condition is 10.0 nm. An alternating fluid delivery is applied in a dynamic sensing experiment with syringe pump controlled ratios of water and oil. Excellent agreement between the measured data and the video images of fluidic streams in the optofluidic cell is found.

OCIS codes: (130.6010) Sensors; (350.4238) Nanophotonics and photonic crystals; (280.4788) Optical sensing and sensors.

References and links

1. T. W. MacDougall and P. E. Sanders, "Large-diameter waveguide Bragg grating components and their application in downhole oil and gas sensing," Proc. SPIE **5589**, 221–232 (2004).
2. N. G. Skinner and J. L. Maida, Jr., "Downhole Fiber-optic Sensing: The Oilfield Service Provider's Perspective," Proc. SPIE **5589**, 206–220 (2004).
3. R. Bont, D. Inaudi, and R. Walder, "Detection and localization of leakages in toxic/flammable chemicals pipelines using distributed fibre optic sensors," Chem. Eng. Trans. **36**, 31–36 (2014).
4. S. K. Khijwania, V. S. Tiwari, F. Y. Yueh, and J. P. Singh, "A fiber optic Raman sensor for hydrocarbon detection," Sens. Actuators B Chem. **125**(2), 563–568 (2007).
5. P. Thoniyot, F. E. Cappuccio, S. Gamsey, D. B. Cordes, R. A. Wessling, and B. Singaram, "Continuous glucose sensing with fluorescent thin-film hydrogels. 2. Fiber optic sensor fabrication and in vitro testing," Diabetes Technol. Ther. **8**(3), 279–287 (2006).
6. M. Benounis, T. Aka-Ngnui, N. Jaffrezic, and J. P. Dutasta, "NIR and optical fiber sensor for gases detection produced by transformation oil degradation," Sens. Actuators A Phys. **141**(1), 76–83 (2008).
7. Y. P. Sharkany, I. I. Trikur, S. A. Korposh, and J. J. Ramsden, "Sensitive elements based on bacteriorhodopsin for fiber–optics sensors of chemical components," Proc. SPIE **5855**, 411–414 (2005).
8. G. Tsigaridas, D. Polyzos, A. Ioannou, M. Fakis, and P. Persephonis, "Theoretical and experimental study of refractive index sensors basedon etched fiber Bragg gratings," Sens. Actuators A Phys. **209**, 9–15 (2014).
9. T. C. Oates and L. W. Burgess, "Sensitive Refractive Index Detection Using a Broad-Band Optical Ring Resonator," Anal. Chem. **84**(18), 7713–7720 (2012).
10. Y. Liu and H. W. M. Salemink, "Photonic crystal-based all-optical on-chip sensor," Opt. Express **20**(18), 19912–19920 (2012).
11. Y. Liu and H. W. M. Salemink, "All-optical on-chip sensr for high refractive index sensing," Appl. Phys. Lett. **106**(3), 031116 (2015).
12. Y. Akahane, T. Asano, B. S. Song, and S. Noda, "High-Q photonic nanocavity in a two-dimensional photonic crystal," Nature **425**(6961), 944–947 (2003).
13. Y. Akahane, T. Asano, B. S. Song, and S. Noda, "Fine-tuned high-Q photonic-crystal nanocavity," Opt. Express **13**(4), 1202–1214 (2005).
14. B. Song, S. Noda, T. Asano, and Y. Akahane, "Ultra-high-Q photonic double-heterostructure nanocavity," Nat. Mater. **4**(3), 207–210 (2005).
15. T. Asano, B. S. Song, and S. Noda, "Analysis of the experimental Q factors (~ 1 million) of photonic crystal nanocavities," Opt. Express **14**(5), 1996–2002 (2006).
16. C. Kang, C. T. Phare, Y. A. Vlasov, S. Assefa, and S. M. Weiss, "Photonic crystal slab sensor with enhanced surface area," Opt. Express **18**(26), 27930–27937 (2010).
17. Y. Liu and H. W. M. Salemink, "All-optical on-chip sensor for high refractive index sensing in photonic crystals," Europhys. Lett. **107**(3), 34008 (2014).
18. http://ab-initio.mit.edu/wiki/index.php/Meep

#282358 https://doi.org/10.1364/OE.25.017201
Journal © 2017 Received 6 Dec 2016; revised 18 Jan 2017; accepted 18 Jan 2017; published 11 Jul 2017

Optics EXPRESS

19. Y. Akahane, T. Asano, B. S. Song, and S. Noda, "Fine-tuned high-Q photonic-crystal nanocavity," Opt. Express **13**(4), 1202–1214 (2005).

1. Introduction

In the recent decade, the advantages of sensing with optics are more obvious than ever before. Optical sensors have been widely used in fields of biological/medical diagnostics, chemical detection, environmental monitoring, national defense and civil engineering. Unlike most of traditional electrical sensors, optical sensors are smaller in size and immune to electromagnetic interference, and are easily integrated in fiber networks. Two main categories of optical sensing are discernible as direct and indirect sensing. Indirect sensing utilizes derivative techniques to convert physical parameters such as pressure [1,2] or temperature [3] to analytes. Indirect sensing is widely used in fields where harsh working conditions or contaminate problems are very commonplace. Direct sensing is usually used in relatively safe environment. Compared to indirect sensing, direct sensing is on average more precise, since the analyte material itself is involved in the process of light-matter-interaction resulting in more accurate detection. Raman scattering effect [4], fluorescence spectra [5], and changes of refractive indices are typical methods for direct sensing. Usually, chemical related sensing relies on interactions between analytes and receptors coated on the sensors [6,7]. Sensitivity and response time of such sensors depend greatly on capabilities of receptors, which usually require the response-time and the recover-time from tens of seconds to a few days. The sensing methods that relate to physical effects are relatively easier to apply than those with chemical reactions. Input light or evanescent light directly interact with analytes and senses their refractive indices with spectral variations. Since no adjustment time for effective chemical reactions is needed, a faster response time is gained. A key factor in enhancing sensitivity of such sensors is to increase the light-matter interaction. For fiber-bragg-grating (FBG) sensors, longer grating structure and etched-down cladding [8] are typically used to enhance interactions. Similarly, for ring-resonator based sensors, a larger ring diameter might be chosen [9]. Nevertheless the scales of such sensors hinder wide applications in fields where limited amount of analytes are allowed or extremely small device dimensions are required.

In our earlier work, we have used nanophotonic cavities in two-dimensional silicon photonic crystals (PhC) for the purpose of refractive index sensing with enlarged interacting volumes from additional mini holes [10] and nano-slots (50 nm in width) [11]. These cavities with a scale of several microns accumulate large number of photons attributed to the resonances in the cavity of the photonic crystals. In most of these works, the analyte (fluids or gas) has infiltrated the holes and the slots of the crystal, and thus directly interacted with the confined resonant light. It has turned out by our simulation that these nanophotonic sensors perform as well as FBG sensors and ring resonators in sensing under same conditions [8,9], and these are fabricated predictably and reliably by using nanofabrication technology.

Although refractive index sensing has no selectivity to chemical compositions, it can be perfectly accepted in applications where analytes are naturally separated, such as flows containing gas, water and oil. The sensor can be used to monitor distributions and ratio of each phase. In this work, we have created an optofluidic chip with integrated optical sensors and the fluidic channel. By modifying structural parameters of optical cavities, higher output intensity and higher sensitivity of the sensor are achieved even under the situation of oil-wetted-surfaces. A prototype of monitoring the real-time ratios of water and oil in the optofluidic cell is realized.

2. Design

Photonic crystal cavities are typically designed with either air-bridge structures [12–16] or with supporting layers underneath. For gas related sensing, air-bridge structures are in general used to gain higher quality factors [10] for finer sensing-resolution. On the other hand, for

Optics EXPRESS

liquid sensing one usually keeps the supporting layer to maintain mechanical stability [11,17]. Apart from the problem of low-index-contrast between silicon photonic crystals and fluidic analytes as discussed in one of our previous works [17], a clean surface of silicon chip is often wetted by residual oil in real cases. Residual oil on the top surfaces of chips can be gradually thinned in flow by following fluids, while stagnant oil stuck in the etched fine structure of photonic crystals can hardly be removed by rinsing with the second fluid in a short time due to the wetting capability.

The PhC cavity (with a triangular lattice) is designed in a two-dimensional slab and illustrated in Fig. 1(a). The cavity was designed for working in near-infrared wavelength region around 1550 nm. Therefore, the material of the slab was chosen to be silicon and the underneath supporting layer was chosen to be silicon dioxide. The cavity is created by skipping three holes in the Γ-K direction and surrounded by 10 and 12 rows of holes in the Γ-K and Γ-M directions. The thickness of the silicon was $h = 0.44a$ (a is the lattice constant), and the thickness of the silicon dioxide was $4a$.

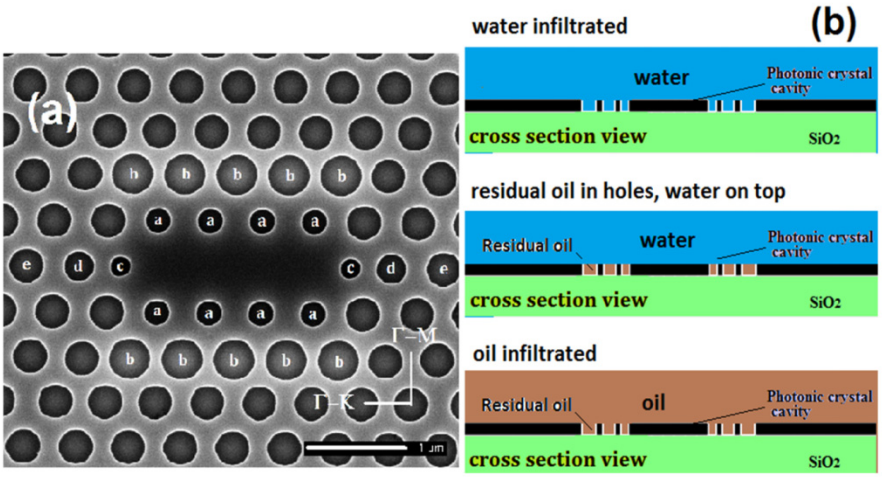

Fig. 1. (a) Scanning electron microscope image of the photonic crystal cavity. Modified holes are marked in the image. Lattice constant $a = 500$ nm. $r_a = 0.7r$, $r_b = 1.1r$, $r_c = 0.6r$, $r_d = 0.9r$, and $r_e = r$. (b) Schematic cross-sectional images of the three situations in sensing oil and water.

To simulate effects of residual-oil, holes of the photonic crystal used in simulation were filled with a material which has a refractive index close to residual oil, as depicted in Fig. 1(b). Intrinsic quality factors and intensities (after 400 time-steps after excitation) of resonant modes were calculated by the three-dimensional finite different time domain (FDTD) simulation program of MEEP [18] developed by the MIT group. Figure 2(a) and 2(b) present simulated resonance of the cavity with different filling-fractions (size of holes) of photonic crystal. Clear resonances are observed as the filling-fraction varies from $r = 0.33a$ to $r = 0.37a$. The maximum quality factor and the highest intensity were obtained at $r = 0.35a$. Further optimizations were done on holes close to the cavity as marked in Fig. 1(a). Gradual increasing sizes of holes from hole-c to hole-e ensures the optical field of the resonant mode with Gaussian distribution in the Γ-K direction [19], which is also the wave vector direction. In Γ-M direction, sizes of the closest holes (hole-a) were reduced to create larger area for high-index-material (silicon) to accumulate more photons. Enlarged holes of type b-hole were used to provide a better prevention for the confined photons from leakage. As a result the optimized cavity did perform as sensitive as our previously published cavity-designs in the wavelength shifts. The transmission spectra of sensors with different filling-fractions were given and analyzed in the simulations of Figs. 2(c)-2(e).

Optics EXPRESS

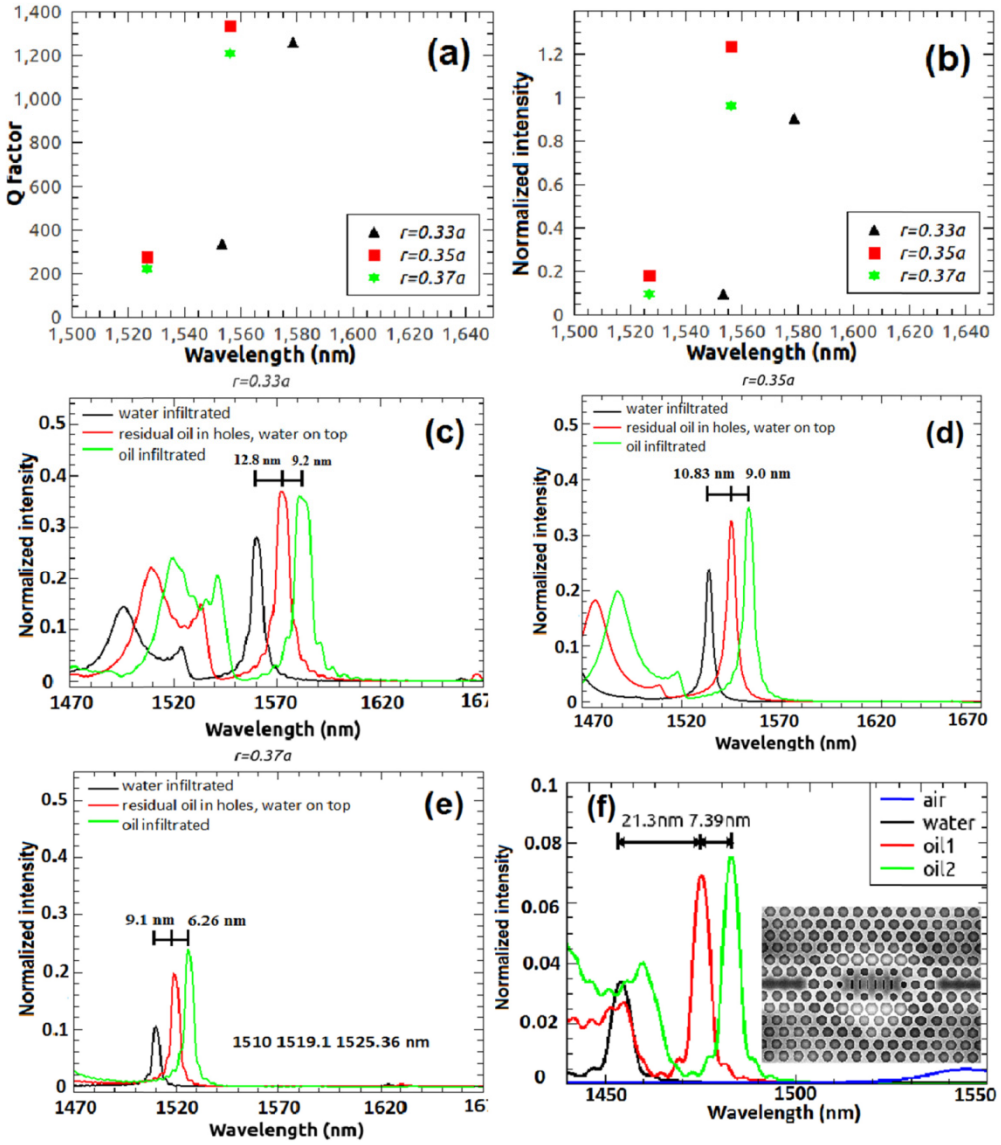

Fig. 2. Simulated intrinsic quality factors (a) and normalized intensity (b) of cavities with different filling-refractions of photonic crystals from $r = 0.33a$ to $r = 0.37a$. (c), (d), (e) Simulated wavelength shifts among the three situations: (c) $r = 0.33a$ with a total $\Delta\lambda = 22$ nm. (d) $r = 0.35a$ with a total $\Delta\lambda = 20.5$ nm (e) $r = 0.37a$ with a total $\Delta\lambda = 15.4$ nm. (f) Previous simulated result of wavelength shift from a sensor designed with inner slots in a cavity [11]: A wavelength shift of 21.3 nm was calculated between water/oil infiltrations.

The process of sensing was simulated in three different situations as shown in Fig. 1(b). The first situation had no oil in the sensor and the hollows of the photonic crystal are infiltrated by water only. The refractive index of water is set to 1.33. In the second situation, the holes of photonic crystal were filled with stagnant oil but there is no residual oil on the top surface of the silicon slab. The residual oil has a refractive index of 1.50. In the third situation, the sensor was completely infiltrated and covered by oil. The sensitivities of sensors were reflected by wavelength shifts for the three situations. Sensors with filling-fraction of $r = 0.33a$ and $r = 0.35a$ had larger wavelength shifts of ~20 nm than $r = 0.37a$ among the three situations. Although the intensities of resonant peaks between $r = 0.33a$ and $r = 0.35a$ were

Optics EXPRESS

comparable, higher quality factors were found at $r = 0.35a$. The intrinsic sensitivity of the sensor is ~117 nm/RIU (refractive index unit). These spectral properties in Figs. 2(c)-2(e) matched with simulated Q factors and intensities presented in Figs. 2(a) and 2(b). More importantly, the wavelength shift between situation 2 and situation 3 was as large as 9.0 nm at $r = 0.35a$, which enabled a monitoring of flow even with oil-wetted surfaces of the sensor.

3. Sensor fabrication and measurements

The realization of the sensor involves two main steps: (a) fabrication of the photonic cavity and (b) fabrication of the aligned fluidic channel. The photonic crystal sensor was realized on silicon-on-insulator (SOI) wafer with a 220 nm-thick silicon slab and a 3 μm-thick silicon dioxide insulator layer. Fabrication started from cleaning a 4 cm^2 SOI chip with nitric acid to remove residual organics. ARP6200.09, a positive electron-beam resist, was spun on the SOI chip with an approximate thickness of 200 nm followed by a pre-baking at 150 °C for 3 minutes. The photonic crystal was patterned using a Leica EBPG 5200 e-beam lithography system operating at 100 keV. Exposed areas of the SOI wafer were then etched by SF_6 and O_2 plasma using the inductively coupled plasma (ICP) dry etching at the temperature of –120°C. Following the ICP etching, the remaining e-beam resist was dissolved in acetone. Isopropyl alcohol (IPA) was used afterwards to remove surface contaminants. After rinsing 3 times with de-ionized water, the chip was dried by nitrogen gas. An image of the photonic crystal cavity taken by a scanning electron microscope is presented in Fig. 1(a). Typically, we fabricate 3-10 photonic cavities (including access waveguides) on one chip with good repeatability in structure.

The second part in fabrication is the fluidic chip to be aligned over the optical cavity. For easy replication, a mold of fluidic channel was first made on a 4-inch silicon wafer by micro optical lithography. The channel had two input-ports which were connected at a T-shape junction on one side of the channel, shown in the inset of Fig. 3(b). On the other side, an output-port was designed to collect liquid wastes. The pattern of the fluid channel was transferred to silicon wafer by deep Bosch etching after lithography. A polymer material-polydimethylsiloxane (PDMS) was then poured on the silicon mold and cured at 70 °C for 1 hour to turn liquid PDMS to solid. The channel was carefully peeled off and punched to open accesses to those ports from outside. After thoroughly cleaning with ethanol and de-ionized water, the PDMS channel was treated with O_2 plasma to create a hydrophilic surface. Rapid visual aligning and pressurized bonding between the sensor chip and the fluid channel must be applied within a few minutes after the plasma treatment. The bonded chip was then baked at 150 °C for 2 hour to enhance the bonding strength.

As shown in the inset of Fig. 3(a), a pair of photonic crystal waveguides was created by introducing single mode light path in the Γ-K direction of the photonic crystal. Coupling light into/out of the sensor was accomplished by traditional strip waveguides. The strip waveguides tapered from 2 μm from edges of the chip to $\sqrt{3}a$ at the interface of the photonic crystal waveguides. Finally, the strip waveguides were exposed to fiber-coupling at the end-facets by cleaving.

Optics EXPRESS

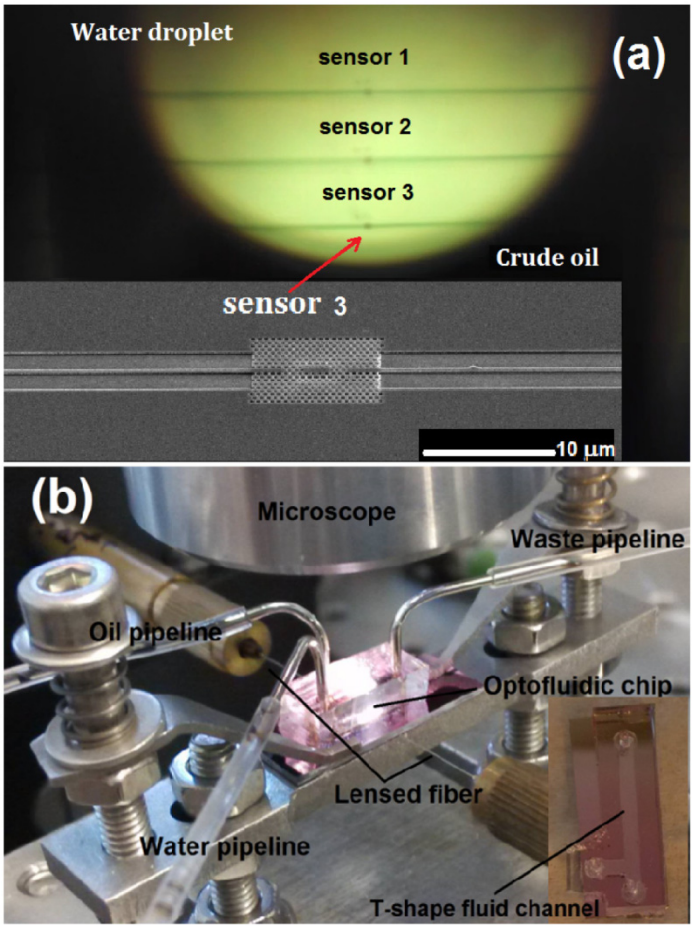

Fig. 3. (a) A view of water/oil droplets covering the sensor. Note: three sensors are imaged by the microscope. Inset: a SEM image of a cavity on the chip with strip waveguides. (b) Experimental set-up. Inset: a T-shape fluid channel bonded on a sensor chip. The cavity of the sensor is below the channel.

The opto-fluidic (silicon-PDMS) chip was fixed on a 5-axis sample-holder. A pair of polarization-maintained lensed fibers was placed on piezo-controlled 3-axis optical stages with fine adjustment as shown in Fig. 3(b). Transverse electromagnetic (TE) modes were kept in fibers with extinction ratios over 100:1. Two digital syringe pumps served as analyte-reservoirs to inject liquid from the two input ports of the fluid channel. A high magnifying lens connected to a microscope image system was mounted above the sensor chip to capture movie clips of the moving fluids (oil/water). Clear views of the sensor under the fluid channel can be observed during measurements as illustrated in Fig. 3(a), and dynamic video clips of these views were recorded as real-time proofs. Light from a tunable laser (Tunics T100S-HP) ranging from 1500 to 1680 nm propagated through input fiber and was coupled to the input strip waveguide. Output light from the output strip waveguide was collected by the output fiber and finally transmitted to a sensitive photon detector. We recorded data at resonant wavelengths of oil from the photon detector and analyzed these data with simultaneous video clips.

In the first step, the features of the sensor were measured with independent analyte-flow (water or oil). Water used in the experiment was directly from a common water-tap, and oil measured here was crude oil. According to our studies, a clean surface of silicon is super-

Optics EXPRESS

oleophilic. The contact angle of an oil droplet on silicon surface is nearly 0°, which means subtle structures fabricated on silicon chips are always filled with stagnant oil in the test. The stagnant oil can hardly be removed by rinsing the sensor with water. An ideal situation of water-infiltration shown in Fig. 1(b) doesn't exist in real applications of mixed oil and water flow. Our measurement was first taken for oil-flow, then for water-flow. We use this sequence to display the influence of the stagnant oil stuck in holes on the sensitivity of the sensor.

Transmission spectra were plotted in Fig. 4. The red line, which corresponded to oil-flow-infiltration, shows a resonance at 1554 nm. The black line corresponded to water-flow, but the sensor was already filled with residual oil in holes. Since the cavity is designed of higher intensity as higher-refractive-index material infiltrated, output intensity of the water-flow-covered sensor was not as high as with an oil-flow infiltration, but a clear resonance is still observable around 1544 nm. Another reason for a higher output of oil in Fig. 4 was less transmission loss in waveguides. The stripe waveguides shown in Fig. 3(a) were actually exposed to analytes during the tests. The refractive index of oil is closer to the refractive index of the PDMS (~1.5-1.6) than water, and resulted in less index-mismatch-caused loss at the left and right boundaries of the channel, which were firmly bonded on the silicon chip and in direct contacts with stripe waveguides. We have embedded the sensor and waveguides in protecting materials and observed intensity contrasts between water and oil contact matched simulations. Detailed discussion on embedding sensors in protecting materials will be presented separately from this paper. A wavelength shift of 10.0 nm between the two conditions was obtained with our current sensor, which is in good agreement with the simulation result of 9.0 nm as discussed in the previous section.

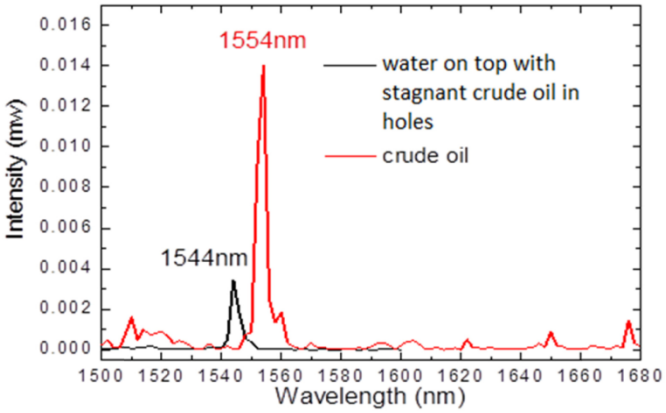

Fig. 4. Measured transmission spectra of water and oil flow atop the sensor. The wavelength shift between water and crude oil contact is 10.0 nm of the sensor with stagnant oil in holes, which is very close to the simulation result of 9.0 nm in Fig. 2 (d).

In the second step, real-time variations of oil ratio in water flow were programmed by syringe pumps. The two input ports of the fluid channel were connected to syringe pumps via small pipelines (Fig. 3(b)). Due to surface tension between water and oil, alternating droplets of water and oil are formed at the T-junction of the fluid channel. Droplets moved in the fluidic channel and get in contact with the sensor as filmed in the dynamic video clips in Fig. 5 of Visualization 1 and Visualization 2 (three sensors were illuminated on the chip. we have used the third one). By changing size and repeatability of droplets, we adjusted real-time ratios of oil in the water flow.

In the measurement presented in this paper, we have recorded both output light from the sensor and simultaneous video clips of droplets in the flow for about 4 minutes. During the test, we decreased the ratio of oil to water roughly from 7.5:1 to 1:1. Two short clips of video

Optics EXPRESS

are shown in Visualization 1 and Visualization 2 in Fig. 5 with different flow ratio. The input laser wavelength was fixed at 1554 nm, which is the resonant wavelength with oil-infiltrations. Therefore, the sensor switches alternatively between on-resonance and off-resonance as oil and water droplets cover its top-surface. The output intensity was accordingly varied between high and low values. In Fig. 6(a), the output intensity is plotted by the black curve. Two shadow areas without data were moments that we adjusted ratios from injection rates of syringe pumps. Figures 5(a) and 5(b) were clips of the flow in section 1 and section 3 of Fig. 6 with different ratios. Areas encircled by red-rectangular in Figs. 6(b)-6(d) represent the window where oil droplets flowed over the sensor in video clips. Gaps among those areas were water droplets flowing atop the sensor. Zoom-in details of each section of Fig. 6 provide clear evidences for the functionality of the sensor. In the entire 4 minutes of measurement, each period of high intensity output corresponded to a single oil droplet covering the sensor. As ratio varied from 7.5:1 to 1:1, time-ratio between high-intensity area and low intensity area also varied synchronously. It is noticed that contrasts between high and low output intensity of the sensor are not constant in value. Actually, this contrast diminishes gradually during the observation time. This phenomenon is caused by a thickened residual oil film on the top surface of the silicon slab. Our simulation have shown red-shifted resonant wavelengths as the thickness of the residual oil film increases, which are reflected in lowered contrasts in intensities between water and oil contacting. As we have mentioned in the "design" section of this paper, the residual oil on the top surface of the silicon can be removed by rinsing the sensor with large amount of water. In one of our tests, intensity contrast has been increased to more than 95% with an individual water flow velocity up to 150 mm/s. However, it is still difficult to completely remove the residual oil with moderate flow velocities of water in a short time. Admittedly, the residual oil on top of the silicon can degrade the resolution of our sensing, but chemical treatment, which can create less oleophilic surfaces on silicon slabs, will alleviate this effect. This work is underway and will be discussed in a separate paper.

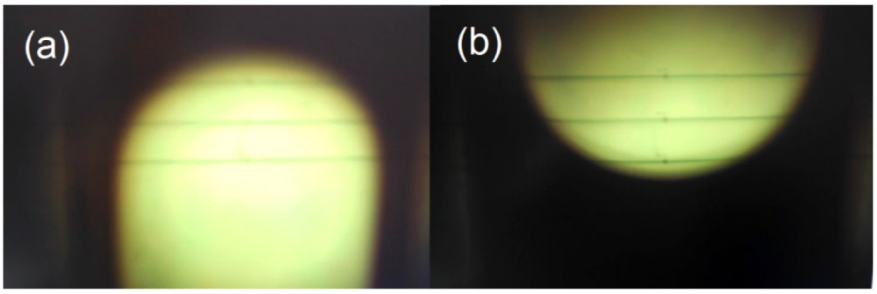

Fig. 5. Short video clips from the experiment of dynamic ratio-monitoring. There are three sensors in the view (black waveguides and black center spot (cavity)); we use the third cavity to monitor the ratio. (a) Video clip of section 1 (see Visualization 1). Oil-contact had longer time than water-contact; (b) Video clip of section 3 (see Visualization 2). Oil-contact and water-contact were nearly equal in time.

Since the sensor is sensitive to analytes flowing above, therefore in a continuous flow, a threshold level is necessary to time the beginning and end of each oil/water droplet in order to read ratios of oil and water. The threshold level is the increase (in percentage) of the two bottom-intensities of each peak in the output curve caused by the replacement of water to oil. Data with intensity higher than the threshold level are considered as oil-droplet-contact. Contrarily, data with lower intensity than the threshold level is recorded as water-droplet-contact. Selection of the threshold level was determined by velocity, viscosity of the analytes and their interactions with surfaces. These characteristics are also reflected in the profile-shape of the intensity curve. As ratio of oil to water decreases, the output intensity gradually turns from rectangular wave-like curve to sharp-angled wave-like curve. (Hydromechanical

Optics EXPRESS

reasons behind this phenomenon will be discussed in separated papers.) In our experimental based statistics, for rectangular-wave-like curves, higher thresholds (≥40% intensity increase) fit well with real flow monitored by video camera, and for curves with sharp-angles, lower thresholds (<40% intensity increase) are used. Based on these rules, we have analyzed the output intensity in Fig. 6.

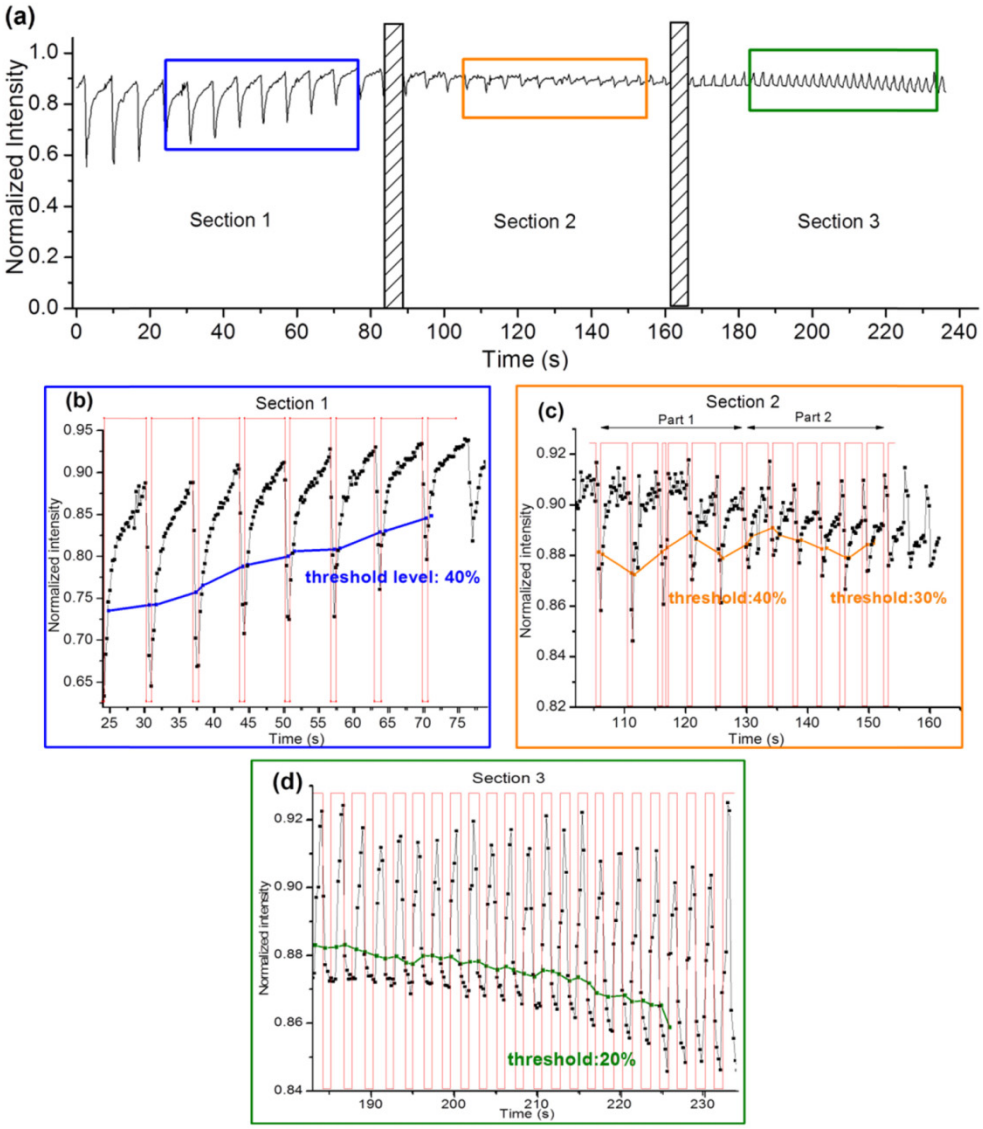

Fig. 6. (a) A real-time dynamic sensing of continuously alternating water/oil flow in 4 minutes. A very clear pattern emerges for the alternating water/oil flows. The selection of a threshold assists in determining the ratio-changes in analyte. Note the clear distinction between oil and water in all cases. (b) Detail of section 1 in the measurement. A threshold level of "40% increase in intensity" is given to fit the beginning and end of oil droplets. (c) Detail of section 2. Two threshold levels of 40% and 30% are given to the two parts in section 2 separately because of the adjusted input rate of analytes. (d) Detail of section 3. A much lower threshold of 20% is used. From section 1 to section 3, the intensity-contrast diminished gradually during the observation time due to a thickened residual oil film on the sensor chip.

Optics EXPRESS

The first section of data in Fig. 6 had profiles similar to rectangular wave. We run fitting based on our hydromechanical theory and experimental statistics, and set the threshold of "40% intensity increase of bottoms (the blue line in Fig. 6(b))" to show time of oil droplets covering the sensor. Because of the adjusted injection rate of analytes at the end of section 1, analysis on the profiles of the curve in section 2 were separated into two parts. Time delay between the adjustment and the change of curve was caused by the flowing time in pipelines. We kept the threshold as "40% (increase in intensity)" for the anterior part, and decreased the threshold to "30%" for the posterior part where "right-sides" of peaks were abruptly higher and rectangular-wave-like curve tended to sharp-angled-wave-like curve. Threshold levels of the two parts were marked by orange lines in Fig. 6(c). After adjusted injection rates again before section 3, curve in section 3 showed the typical profile of a sharp-angled-wave. The threshold level given to this section was decreased to "20% increase of bottom-intensities" (the green line in Fig. 6(d)). The ratios of the three sections were summarized in Table 1. Ratios read by the sensor were in excellent agreement with video clips. We notice that the threshold level has played an important role for calculating the oil ratio in water. For further and detailed analysis, the issues of viscosity, surface tension, wetting and friction will be discussed in a further paper. Surface treatment will be used to adjust these parameters. We will compare the performances of sensors with different (silane) treatment for oleophobic/hydrophilic surfaces, compare contact angles before and after treatment, analysis flow velocities and reveal hydromechanics in the sensing systems and their impact on the threshold levels.

Table 1. Comparison of dynamic ratio of oil and water observed in the video clips and in the output intensity

	Section 1	Section 2		Section 3
		Part 1	Part 2	
Average ratio of "oil:water" from video clips	7.41:1	4.54:1	3.58:1	1.27:1
Average ratio of "oil:water" from output intensity	7.7:1	4.09:1	3.38:1	1.25:1
Deviation between the above two groups of data	+ 0.039	–0.099	–0.055	–0.016

4. Conclusion

We demonstrate the real-time monitoring of water and oil flows with a photonic crystal cavity based sensor embedded in an optofluidic cell. We discern very clear resonances and track the oil resonance during alternating flow cycles between oil and water. With the good cavity design of residual-oil-in-sensor, we obtain good reproducibility and very accurate prediction of resonance shifts of 10.0 nm in experiment and 9.0 nm in 3D simulations. Swift and reliable monitoring for dynamic flows is obtained with good thresholds. As the sensor is robust in design and fabrication, we envisage using it in oil wells as well as in medical testing, by using surfactants and arrays in future.

Funding

Shell Global Solutions of Nanophotonic Sensors (NPS).

Acknowledgments

Many appreciations are given to Juun van der Horst, Cor Kruijsdijk from Shell E&P, William Rossen, Jan-Dirk Jansen, Michiel Slob from Petroleum Engineering, Delft University of Technology, and Tonnie Toonen from Radboud University.